Shallow Aseismic Slip in the Delaware Basin Determined by Sentinel-1 InSAR

K. S. Pepin[1], W. L. Ellsworth[1], Y. Sheng[1,2], and H. A. Zebker[1]

[1]Stanford University Department of Geophysics

[2]Institut des Sciences de la Terre, Université Grenoble Alpes, Grenoble, France

Corresponding author: Karissa Pepin (kspepin@stanford.edu)

Key Points:

- Surface deformation in the southeastern portion of the Delaware Basin can be attributed to aseismic slip on normal faults within the Delaware Mountain Group
- Identified faults create graben structures that likely belong to a larger graben network
- Aseismic and seismic fault movement in Texas' Delaware Basin can be linked to wastewater injection in the Delaware Mountain Group

Abstract

The Delaware Basin, Texas is currently a hot-spot of induced seismicity and ground deformation due to fluid extraction and injection associated with horizontal drilling techniques; however, the driving mechanism behind the seismicity and deformation remains under debate. Using vertical and east-west horizontal surface deformation measurements derived from Sentinel-1 InSAR, we show that the subsurface responds differently to oil and gas activity in the northern and southeastern portions of the basin. In the north, where there is little seismicity, deformation patterns display long-wavelengths and equidimensional patterns. In contrast, the southeast region hosts most of the seismicity and displays spatial deformation patterns with narrow linear features that strike parallel to the maximum principal horizontal stress and to trends in seismicity, suggesting movement along normal faults. We model a linear deformation feature using edge dislocations and show that the InSAR observations can be reproduced by slip on normal faults contained within the Delaware Mountain Group (DMG), the formation that hosts local wastewater injection and the majority of earthquakes. Our model consists of three parallel, high-angle normal faults, with two dipping toward one another in a graben structure. Slip magnitudes reach up to 27.5 cm and are spatially correlated with injection wells. Measured seismicity can only explain ~2% of the fault motion predicted by our fault model, suggesting that slip leading to the deformation is predominantly aseismic. We conclude that seismic and aseismic fault motion in the southeastern Delaware Basin is likely driven by wastewater injection near critically-stressed normal faults within the DMG.

Plain Language Summary

In the Delaware Basin, TX, widespread oil and gas operations have been linked to an increase in earthquake frequency and ground deformation. We use satellites to measure the ground deformation and show that the northern and southern portions of the basin respond differently to the pumping and injection of fluids. The southern portion displays narrow linear displacement patterns, whereas the northern region displays wide and equidimensional features. The relationship of the narrow features in the southern portion of the basin to local stress conditions and earthquake locations suggests downward slip on faults. Using analytic models in a small study area, we develop a three-fault slip model that is consistent with ground displacement

measurements, the location and sense of slip of the largest local earthquakes, and wastewater disposal wells. Our findings suggest that wastewater disposal in the Delaware Mountain Group is reactivating pre-existing normal faults, leading to induced earthquakes and non-seismic slip.

1 Introduction

The Delaware Basin is a giant oil and gas field in the Permian Basin, covering an expansive portion (22,000 km^2) of west Texas and southeastern New Mexico (Figure 1a inset). After being heavily exploited in the 20th century via conventional vertical production, 2009 brought a resurgence in oil and gas activity due to the development of organic rich shale beds using horizontal drilling and hydraulic fracturing (a.k.a. 'unconventional') techniques. Similar to what has been observed in oil fields around the world, the Delaware Basin experienced an uptick in seismic activity coincident with unconventional development, leading many seismologists to infer those earthquakes were being induced by the development itself (e.g. Frolich et al., 2016; Skoumal et al., 2020). Consequently, the State of Texas funded deployment of a regional seismic network, the TexNet array (Savvaidis et al., 2019), to better detect the regional seismicity and determine the underlying causes. The network has recorded thousands of small-to-moderate earthquakes in the Delaware Basin since its deployment in January 2017, including a M_W 4.8 event in late March 2020 (Figure 1a). These events are mainly concentrated in the southeastern portion of the Delaware Basin in Reeves county, despite widespread oil and gas activity throughout the basin (Figure 1b).

The low density of earthquakes to the north of the Grisham fault (Figure 1a) is likely due to low pore pressure conditions caused by decades of conventional oil and gas activity prior to the 21st century; however, the geomechanical mechanisms leading to the onset of seismic activity to the south of the Grisham fault since 2009 remain under debate (Dvory & Zoback, 2021; Hennings et al., 2021). Within the seismically active portion of the basin, the dense concentration of old vertical, new horizontal, and disposal wells (Figure 1b) makes it challenging to determine the most probable industrial drivers, since hydraulic fracking, fluid production, and wastewater injection can all lead to induced seismicity (see Schultz et al., 2020; Suckale, 2010; and Ellsworth, 2013, respectively, for reviews on these topics). For instance, hydraulic fracking is considered a major cause of induced events in western Canada (e.g. Farahbod et al., 2015),

71 whereas earthquakes near the Wilmington Field in California have been linked to extreme
72 subsidence and stress changes from oil and gas production (Kovach, 1974). The most-commonly
73 cited mechanism, however, is wastewater injection, where fluid and increased pore pressure
74 propagate to pre-existing faults, reducing normal stress and allowing seismic rupture (Ellsworth,
75 2013). Indeed, in nearby Oklahoma, where there have been a number of large-magnitude induced
76 earthquakes ($M_W > 5$), studies strongly suggest that deep wastewater disposal near basement
77 faults is the driving mechanism (Keranen et al., 2013; Yeck et al., 2017; Grandin, et al., 2017).

78 In the Delaware Basin, the majority of wastewater disposal occurs in the Delaware
79 Mountain Group (DMG), which lies above the producing shales (Wolfcamp) and 3-4 km above
80 the basement in much of the producing portion of the basin (Figure 1c). In addition, there are few
81 publicly-mapped faults in Reeves county and none of them extend from the DMG into the
82 basement. Therefore, it is unlikely that basement faults are being induced to failure by
83 wastewater disposal, as observed in nearby Oklahoma or elsewhere in Texas (Frohlich, et al.,
84 2014; Hornbach et al., 2015; Frohlich et al., 2016) unless poroelastic effects are the dominant
85 mechanism (Zhai et al., 2021). An additional hurdle is the difficulty of linking specific events to
86 any group of wells, due to the large depth uncertainty in earthquake hypocenters. Earthquakes in
87 the southern Delaware Basin in the TexNet catalog range in depth between 0 and 19 km relative
88 to ground surface (Figure 1c), with an average depth of 6 km and mean uncertainty of 1.9 km.
89 Lomax and Savvaidis (2019) studied absolute depth errors in the basin and found a narrower
90 depth range, when a near station provided some depth control but also large uncertainties of
91 approximately 4 to 5 km. Because the average depth separation between disposal wells in the
92 DMG and the production wells in the Wolfcamp is only 1.2 km, the formal uncertainty can move
93 an earthquake from an injection formation to a producing one, or from a producing formation to
94 the basement, and vice versa.

95 Despite these challenges, recent works attribute seismicity in the Delaware Basin to both
96 hydraulic fracking and wastewater injection. Savvaidis et al. (2020) link clusters of events to
97 fracking operations via temporal and spatial correlations and also highlight a causal link between
98 wastewater disposal and seismicity in a few isolated cases where hydraulic fracking could be
99 ruled out. However, in regions where fracking and disposal overlap, it remains challenging to
100 distinguish between the two sources. On the other hand, Skoumal et al. (2020) attributed the

majority of the seismicity to wastewater disposal, with just ~5% of the earthquakes induced by hydraulic fracturing operations. Another recent study uses poroelastic modeling to show that wastewater disposal at selected wells leads to pore pressure changes sufficient to induce earthquakes (Deng et al., 2020); however, they do not yet explain the absence of earthquakes near the majority of disposal wells in the basin, other than to posit that there are no favorably oriented pre-existing fault planes nearby. Zhai et al. (2021) also use poroelastic modeling to hypothesize that basement seismicity could be explained by poroelastic effects due to shallow injection within the DMG, though the evidence supporting earthquakes in the basement remains highly uncertain.

To better understand the geomechanical connections between industry operations and induced seismicity, it is essential to constrain earthquake depths, determine how the subsurface is responding to well activity, and locate faults hosting seismicity. In some instances, addressing one or both of the first two objectives may illuminate the geometry and behavior of unmapped faults. For example, precision earthquake locations and focal mechanisms, and measured surface deformation from co- and inter-seismic displacements can be combined to define faults and determine the sense and magnitude of slip (e.g. Massonnet & Feigl, 1995; Weston et al., 2012). These techniques are especially feasible when investigating shallow, large-magnitude earthquakes, of which there are currently none in the Delaware Basin. Most of the observed events only have $M_W < 4$, making co-seismic deformation analysis challenging, though not impossible (for instance, Staniewicz et al. (2021) have shown ~0.7 cm of co-seismic deformation related to the M_W 4.8 Mentone earthquake (Figure 1a)). Nevertheless, using methods of interferometric synthetic aperture radar (InSAR), a remote sensing technique that measures mm-scale surface displacements at 5-20 m spatial resolution, we will show that deformation in the Delaware Basin defines fault geometries and sheds light on the difference between the northern (non-seismic) and southeastern (seismic) zones of the region.

The use of InSAR to study the Delaware Basin has been growing in recent years. Kim and Lu (2018) used Sentinel-1 InSAR to map spatially isolated deformation signals and attributed them to subsurface causes, including karst dissolution at the Wink Sink and oilfield activity (see also Kim et al., 2019). In particular, the authors identified local instances of production-induced subsidence and injection-induced uplift. Both Deng et al. (2020) and Zhai et

al. (2021) measured one component of deformation (a single Sentinel-1 radar line-of-sight look direction) to analyze the poroelastic pressure changes due to pumping and disposal, and included groundwater extraction as a possible source of subsidence. They also provided a wider look at the general deformation features in Reeves County. Staniewicz et al. (2020) further extended InSAR to the greater Permian Basin, using two overlapping Sentinel-1 passes (two look directions) over the Central Basin Platform and the eastern half of the Delaware Basin. They noted a significant component of east-west horizontal motion in Reeves and Pecos counties, where the highest density of induced earthquakes occurs. These studies highlight the existence of non-tectonic deformation in the basin and demonstrate that geodesy may be an invaluable tool for understanding the subsurface response to oil and gas operations in this region.

In this paper, we first use Sentinel-1 InSAR to develop a basin-scale look at the vertical and east-west horizontal displacements in the Delaware Basin. The measurements reveal multiple linear deformation zones in the southeastern portion of the basin where seismic activity is concentrated. These features could be a result of slip on normal faults, a possibility that was also explored by Staniewicz and others (2020), though they restricted their modeling to the vertical component of displacement. After motivating the consideration of fault slip, we determine the geometry and slip of potential faults using analytic modeling of both vertical and east-west horizontal displacements, focusing on a small study area along the border of Reeves and Pecos counties (see Figure 1b). We compare our results to an improved seismic analysis in the same study area, which is presented in a companion paper by Sheng et al. (2020/submitted). In that work, they used a moment tensor analysis to determine focal mechanisms and depths for nine moderate events ($M_W > 2.7$), and phase arrival times to determine the depths of smaller earthquakes. When considered together, our study and Sheng et al. (2020/submitted) suggest high-angle normal faults in the Delaware Mountain Group are activated by wastewater injection. We conclude with a discussion of the implications for the nature of induced seismicity in the greater Delaware Basin.

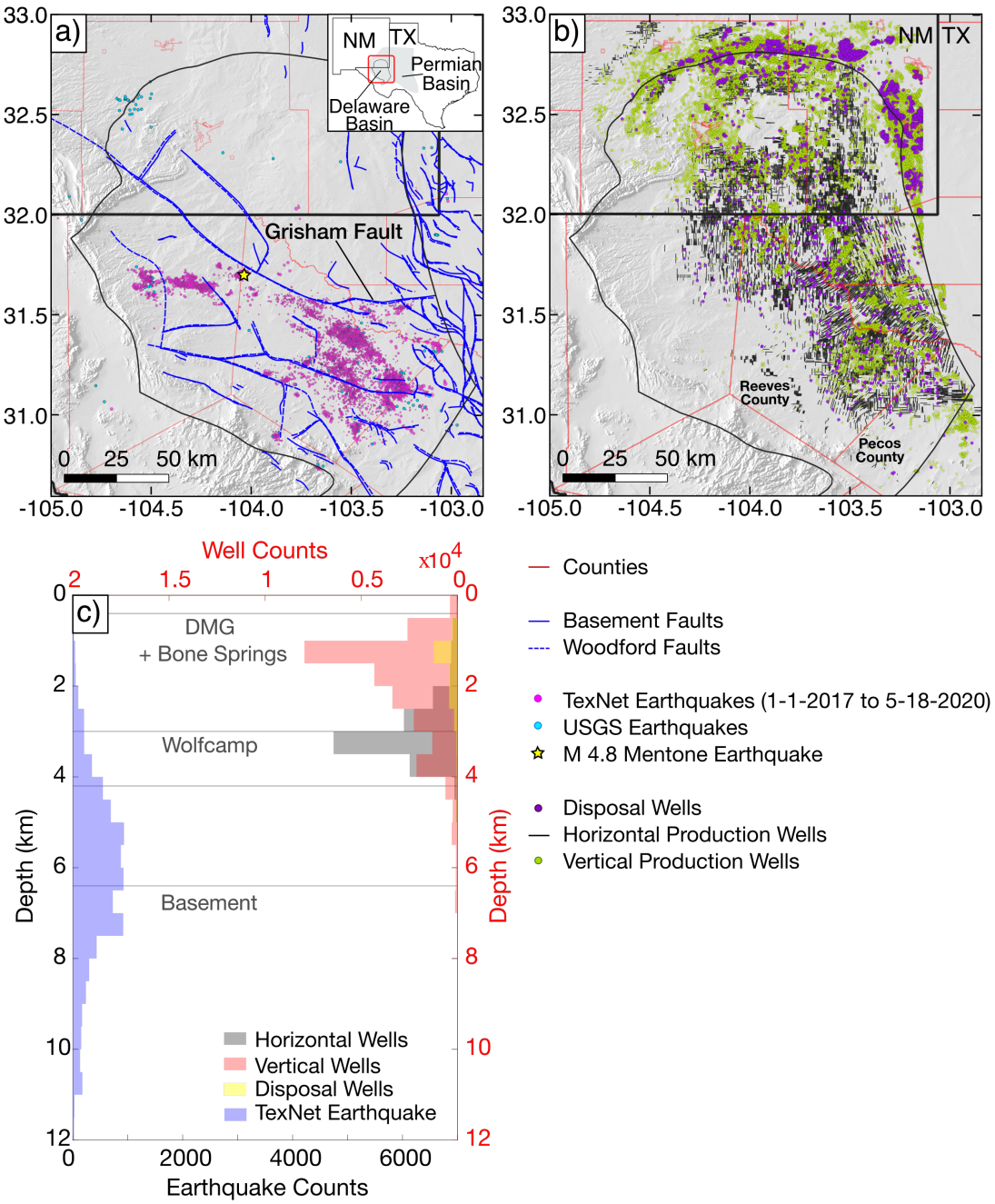

Figure 1. Geology and oil and gas activity in the Delaware Basin. **a** The seismic activity recorded by the USGS and TexNet arrays is concentrated in the southeastern Delaware Basin, below the Grisham Fault. Besides this distinction, few other faults show spatial correlations with seismic trends. **b** shows the disposal and productions wells that were active at some point between Dec 2014-June 2020 and assigned to the Delaware Basin. In contrast to the seismicity, oil and gas activity is widespread throughout the basin. **c** Earthquake depths from the TexNet

164 catalog span a wide range, including into the basement, but these depths are highly uncertain.
165 Most of the injection is concentrated above 3 km depth and above the producing shales. The
166 formation depths depicted in (c) are averages; the true depth ranges vary throughout the basin.

167 2 Sentinel-1 InSAR

168 2.1 Methods: InSAR Processing for Cumulative Displacements

169 The InSAR processing method we use to study the Delaware Basin consists of four main
170 parts. First, we create geocoded single-look-complex (SLC) images at fine resolution
171 (approximately 3.75 m x 15 m) in three orbit sets (ascending paths 151 and 78, and descending
172 path 85; Figure S1), using software developed by the Stanford Radar Group (Zebker, 2017;
173 Zheng & Zebker, 2017). We remove SLCs with high atmospheric noise, resulting in 100 (Path
174 151), 108 (Path 78), and 109 (Path 85) SLCs between December 2014 – June 2020 (Figure S2).
175 Next, we calculate all interferograms formed from SLCs spaced 400 days apart or less, and
176 spatially-average to ~225 m pixel spacing (60 x 15 looks). Then, we unwrap the interferograms
177 using the Statistical-cost, Network-flow Algorithm for PHase Unwrapping (SNAPHU) (Chen &
178 Zebker, 2001) and remove the dry atmospheric phase, as described in Pepin et al. (2020). To
179 determine the cumulative displacement in each look direction, we used a regularized SBAS
180 inversion (Berardino et al., 2002) to create three line-of-sight (LOS) time series, and further
181 reduce the broad atmospheric noise with high-pass filters at each time step (Pepin et al., 2020).
182 In the last stage, we combine and decompose these three data sets into time series of vertical and
183 east-west horizontal displacements.

184 Because we will be jointly analyzing both components of cumulative deformation, this
185 final step warrants a detailed explanation. First, we resample each LOS time series to a uniform
186 set of dates between March 4th, 2015 – March 31st, 2020 with 18 day spacing (Figure S2) and
187 reference each to zero displacement on March 4th 2015. We then combine these two data sets
188 into a "composite" ascending time series by projecting Path 151 onto the LOS unit vector for
189 Path 78, which approximately scales the Path 151 pixels by 0.98, then calculating the arithmetic
190 mean at pixels where the two orbits overlap. We adopt the LOS unit vectors for Path 78 as the
191 composite ascending unit vectors in further analyses. Finally, we decompose the descending and

composite ascending LOS time series into vertical (V) and east-west horizontal (H_{ew}) displacements via the following relationship, which assumes zero north-south motion:

$$\begin{bmatrix} d \\ a \end{bmatrix} = \begin{bmatrix} los_{d-v} & los_{d-ew} \\ los_{a-v} & los_{a-ew} \end{bmatrix} \begin{bmatrix} V \\ H_{ew} \end{bmatrix}, \qquad (1)$$

where d and a are the descending and ascending LOS measurements, respectively, at a single pixel and time step. Descending (los_{d}) and ascending (los_{a}) LOS unit vectors include only their vertical (v) and east-west horizontal (ew) components. We apply Equation 1 to estimate V and H_{ew} at each pixel and time step.

2.2 InSAR Results

We depict cumulative vertical and east-west horizontal displacements between March 4th 2015 – March 31st 2020 in Figures 2a and 2b, respectively. In general, the vertical component is larger than the horizontal counterpart, consistent with previously proposed mechanisms of surface displacement in this region (e.g. poroelastic fluid flow (Deng et al., 2020; Staniewicz et al., 2020) and normal faulting (Staniewicz et al., 2020)). We find that the land surface both rises and falls in the portions of the Delaware Basin where oil and gas activity occurs and is relatively static elsewhere (compare Figures 1b and 2a). We note that the deforming areas include both seismically active and aseismic areas (see Figure 1a). This spatial correlation implies that the deformation can be linked to oil and gas operations, but variations in displacement patterns suggest that different mechanisms may be operating.

In Figure 2c, we modified the scale for cumulative vertical displacement to highlight narrow, short-wavelength linear deformation features in the southern portion of the basin, below the Grisham Fault. These features strike northwest-southeast with a gradual clockwise rotation to the south. In contrast, displacements north of the Grisham Fault have longer spatial wavelengths and no apparent preferred orientation. The horizontal deformation shows a similar regional distinction. To the north of the Grisham Fault, horizontal displacement magnitudes are only up to ~1/2 of the associated vertical magnitudes, but usually <1/4, and form appropriately oriented pairs of east-west displacement around subsidence and uplift features (e.g. westward motion on the right and eastward motion on the left of a subsidence bowl). Below the Grisham Fault,

219 horizontal displacements are typically 1/2 to 3/4 of the associated vertical displacements (in
220 some instances the horizontal even exceeds the nearby vertical), the preferred orientation of
221 features is northwest-southeast, and there are fewer pairs of horizontal displacements around
222 strong subsidence features. Thus, surface deformation in the zones to the north and south of the
223 Grisham fault apparently respond differently to industrial operations.

224 The outlined subregion in Figure 2c corresponds to the highest density of seismic activity in
225 the southeastern quadrant of the basin (Figure 1a), suggesting that the linear InSAR displacement
226 features could be related to the earthquakes. In Figure 3, we display the subregion from Figure 2c
227 to compare these linear features with the tectonic stress field (Figure 2a) and seismicity from the
228 TexNet catalog (Figure 2b). Lund Snee and Zoback (2018) compiled measurements of maximum
229 principle horizontal stress (S_{Hmax}) orientations, depicted as red lines in Figure 2a, and ranked
230 their quality based on the number, depth range, and agreement of measured stress indicators (the
231 authors consider only orientations with A-C ranking sufficiently robust for plotting and analysis).
232 The highest-quality S_{Hmax} orientations ('A' and 'B' lines) are parallel to the linear deformation
233 features. As shown in Figure 2b, seismicity also tends to align with the InSAR deformation
234 patterns. All three data sets independently display the same rotation in strike from ~300° in the
235 northwest corner of the subregion to ~330° in the southeast. Lund Snee and Zoback (2018)
236 classify the stress state of the Delaware Basin as a predominantly normal-faulting regime. Under
237 these stress conditions, normal faults striking parallel to S_{Hmax} are the most-susceptible to fail.
238 Thus, the spatial relationship of these three data sets suggests that slip on pre-existing normal
239 faults is a potential mechanism for the observed deformation in the southeastern zone of the
240 Delaware Basin.

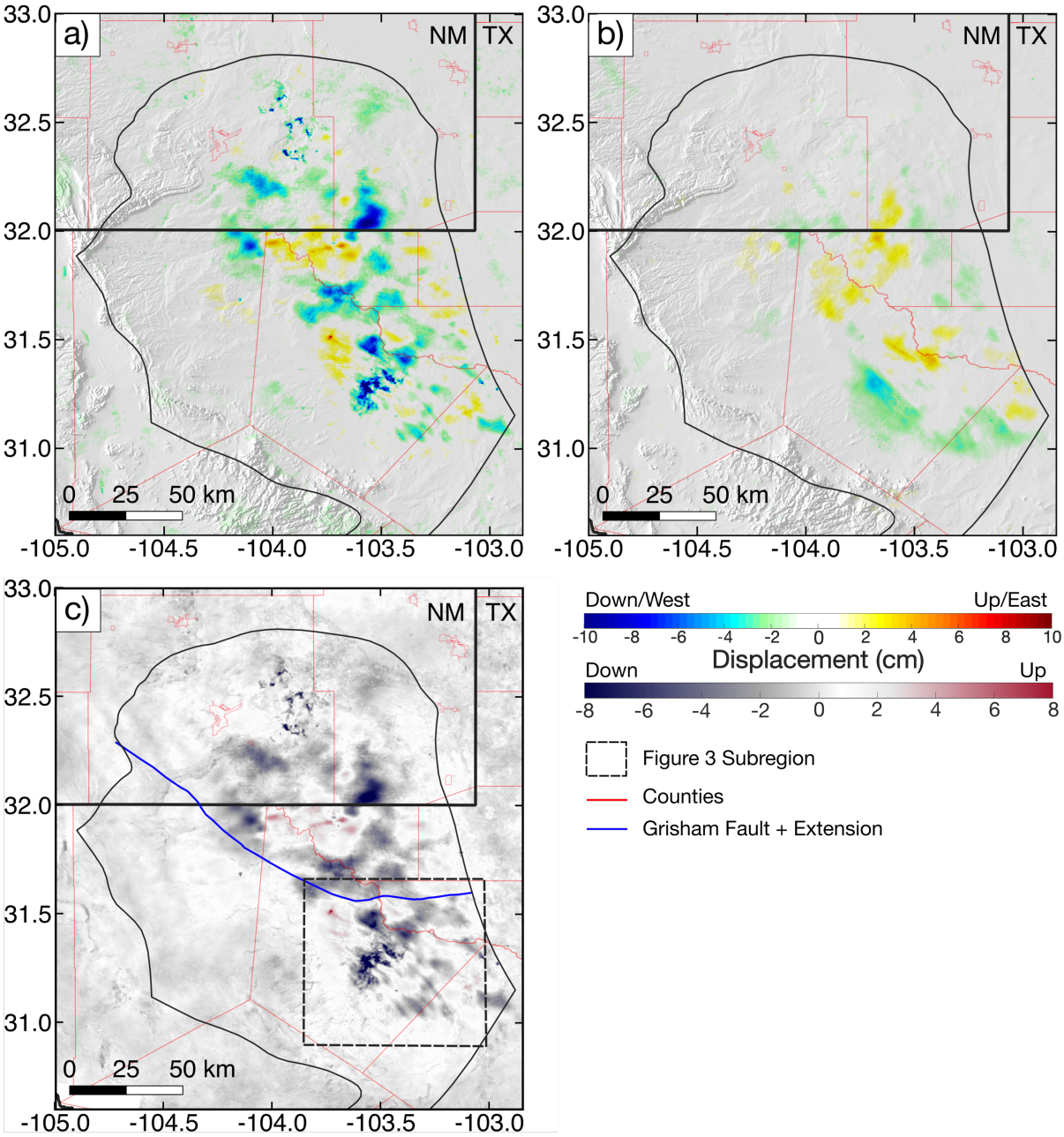

241

242 **Figure 2.** InSAR results in the Delaware Basin. **a** Vertical and **b** east-west horizontal cumulative
243 displacement between March 4th, 2015 - March 31st, 2020. In **c**, we modified the color scale of
244 the vertical displacement to highlight the linear features in the southeastern portion of the basin.
245 Vertical displacements north of the Grisham fault have longer wavelengths and no preferred
246 orientation. In **a** and **c**, warm colors are uplift and cool colors are subsidence, whereas in **b**,
247 warm colors indicate eastward motion and cool represent westward.

248 2.3 Choice of Modeling and Study Area

249 We use an Okada edge dislocation analytic model (Okada, 1985) to test the hypothesis that
250 normal fault slip is the source of linear deformation features in the southeastern zone of the
251 Delaware Basin. In this model the surface displacements are caused by a slipping plane
252 contained within a homogeneous, elastic half-space. Comparing such a fault model with the
253 InSAR displacement field will indicate whether fault slip is a plausible mechanism for the
254 expected i) geometry and location of the planes, and ii) range of slip magnitudes. These model
255 results, however, need to make sense in the larger geophysical context, including the earthquake
256 depths, focal mechanisms, and the spatial relationship of these earthquakes to the deformation.
257 Therefore, to define a suitable study area, we identified a region satisfying the following criteria:
258

259 1. A simple, yet distinct, deformation feature with a clear preferred orientation in vertical
260 and east-west horizontal InSAR components
261 2. Sufficient seismic station coverage to provide accurate focal depths
262 3. Earthquakes large enough to determine focal mechanisms ($M_{W>}$ ~3)
263 4. Deep wells with sonic logs to define the local geologic and velocity structure.

264 The first criterion defines the characteristics of the deformation feature we seek to reproduce
265 using Okada edge dislocations. The latter three criteria address the required accuracy for the
266 earthquake data, if we are to compare the deformation modeling results to seismicity.

267 The study area we selected is outlined by the dashed gray box in Figure 3c. Although there
268 are larger deformations elsewhere nearby (Staniewicz et al. (2020) modeled the area outlined in
269 red), the area we have selected contains a relatively isolated, clear linear feature that exhibits
270 both vertical and east-west horizontal components (Figure 4a and 4b, respectively) in the InSAR
271 measurements, and aligns well with both seismicity from the TexNet catalog and the S_{Hmax}
272 direction. However, the local wells show poor spatial correlation with the expected deformation
273 from fluid volume and pore pressure changes. For example, as described in Text S2 and depicted
274 in Figure S3, there are few production wells (oil or groundwater) collocated with the observed
275 subsidence along the linear feature of interest, and there is little-to-no uplift near active disposal
276 wells. Therefore, explaining this deformation feature needs geomechanical mechanisms other
277 than (or in addition to) radial changes in fluid volume. Also of note is that our selected study area

coincides with the region identified by Teng and Baker (2020) as having the highest seismic hazard in the Delaware Basin. Thus, it is a region of particular importance for operation managers to understand.

We present the related seismic analysis in a companion paper by Sheng et al. (2020/submitted). In our study area, they determined moment tensors for nine events (Table 1) along with the relocation of numerous smaller earthquakes. This analysis used sonic logs from three deep wells in our study area (magenta circles in Figure 3c) to develop the local velocity model that tightly controls earthquake focal depth and moment tensor solutions. Earthquake focal depths concentrate between 1.5 and 3.0 km below ground level, with approximately 80% of the events located in the DMG; fewer than 2% are as deep as the Wolfcamp formation and none locate in the basement. All of the moment tensor solutions are consistent with normal faulting on high-angle planes striking northwest-southeast, with the dip direction split almost evenly between northeast and southwest dips (Table 1). Sheng et al. (2020/submitted) also found no spatiotemporal correlation between fracked wells and the earthquakes, suggesting that they were not induced by hydraulic fracking; rather, they need to be explained by another driving mechanism, such as wastewater disposal, oil and gas production, or perhaps a combination of the two.

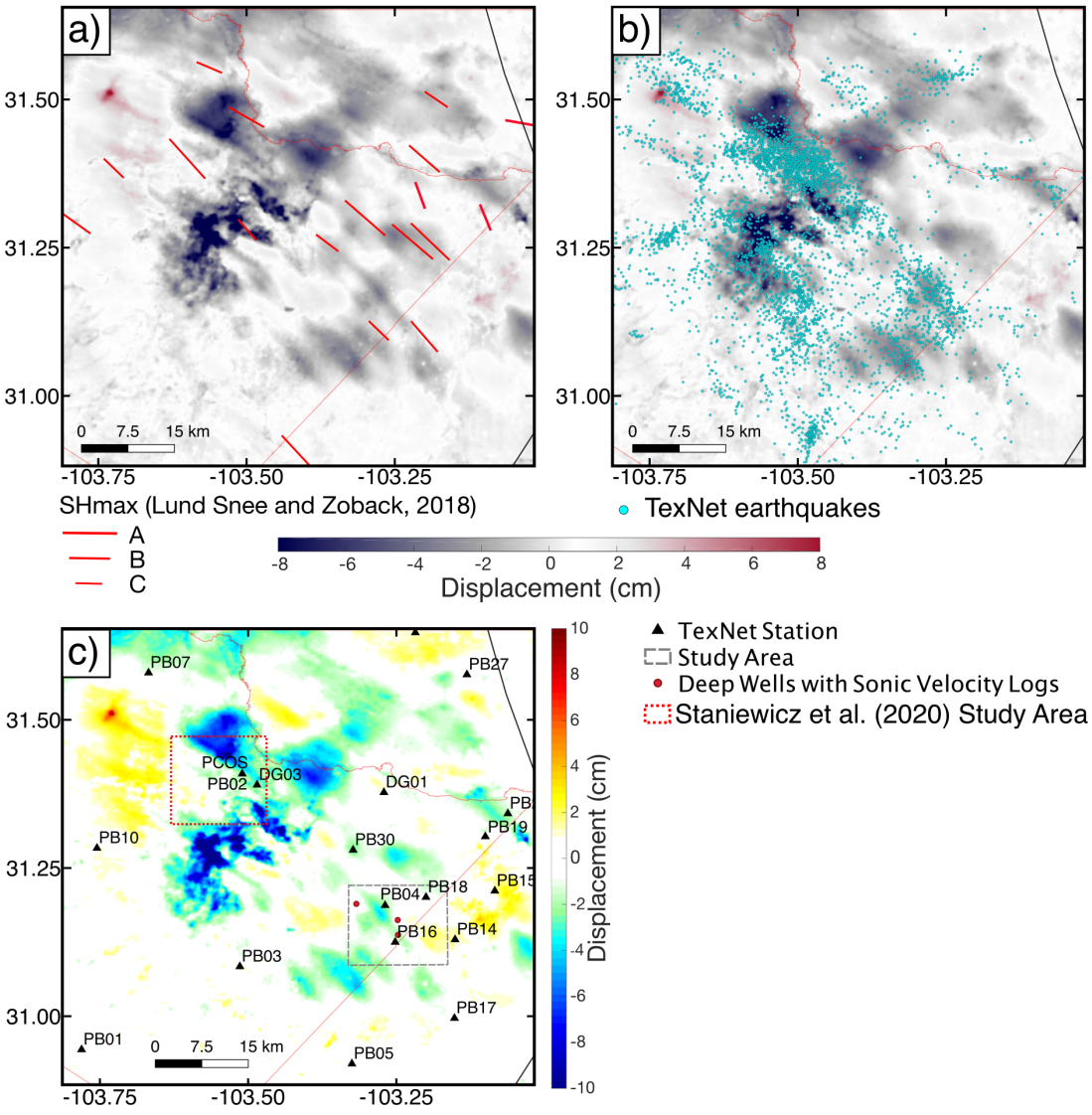

Figure 3. Subregion with saturated color scale comparing linear deformation features to **a** S_{hmax} orientations (Lund Snee and Zoback, 2018) and **b** TexNet events. In **a**, the quality of S_{Hmax} measurement is indicated by the length of the vector, where 'A' is the highest quality, 'B' is good, and 'C' is moderate. We exclude lower-quality measurements from our analysis. **c** shows the subregion with normal color scale. Our study area is the gray, dashed box, with four TexNet stations (black triangles) near moderately-sized earthquakes. Deep wells with sonic logs used to create the 1D velocity model are the red dots.

Hypocenters determined by Sheng et al. (2020/submitted) align with the linear deformation feature in our study area, as shown in Figure 4a and b. The dashed black line delineates the

midline of the displacement feature of interest for initial analysis. Epicenters of the nine events with moment tensors are the numbered black dots, whereas smaller earthquakes determined through conventional location analysis are the gray dots. Earthquakes numbered 1-3 and 6-8 lie along the midline, thus we define them as Group 1, and the relocated smaller earthquakes are densely packed around the same feature. Events 4-5 and 9 (Group 2) form a smaller linear trend to the southwest of the midline, but striking in the same azimuthal direction. In addition, the strikes of the moment tensor solutions are sub-parallel to the azimuth of the midline and earthquake location trends, with predominantly normal slip. We now need to determine whether fault slip can also explain the deformation, if it is consistent with the seismicity, and how it might be related to oilfield activity. The remainder of this paper is devoted to answering these questions.

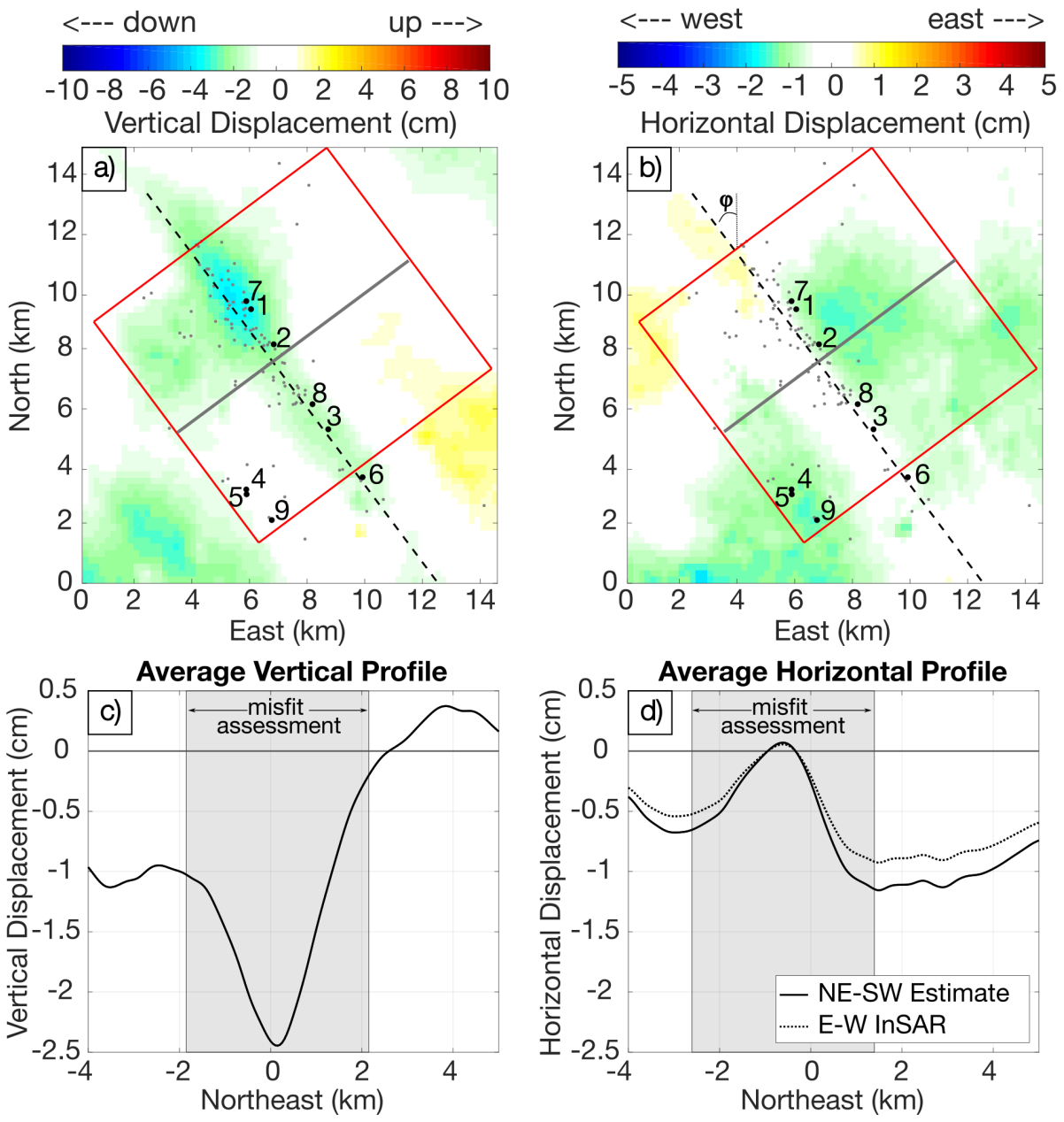

316

317 **Figure 4.** InSAR results in selected study area. **a** Vertical and **b** east-west horizontal cumulative
318 InSAR deformation, with relocated moment tensors (black, numbered dots) and earthquakes
319 (gray dots). Within the red boxes, we calculated the average vertical and horizontal profiles
320 along the gray line, perpendicular to the midline (dashed black line), which we assume to be the
321 azimuth (φ) of the predicted faults. The bottom panel shows **c**, the average vertical profile, and
322 **d**, the average east-west horizontal and estimated northeast-southwest horizontal profiles. During
323 modeling, we calculate the misfit within the shaded gray regions in **c** and **d**.

ID#	Focal depth (km)	Strike	Dip	Rake	M_W
1	2.4 ± 0.1	152	82	-77	2.95
2	1.8 ± 0.2	146	68	-80	2.90
3	2.0 ± 0.2	150	70	-82	2.70
4*	1.4 ± 0.1	326	75	-83	2.84
5*	1.4 ± 0.1	327	74	-82	3.18
6	1.6 ± 0.2	326	70	-81	2.89
7	1.6 ± 0.1	336	63	-76	3.18
8	2.0 ± 0.1	166	81	-65	2.81
9*	1.6 ± 0.1	338	68	-78	2.76

Table 1. Moment tensor solutions (adapted from Sheng et al., 2020/submitted). Stars indicate the earthquakes that belong to Group 2; the others belong to Group 1. All solutions strike sub-parallel to one another and have predominantly dip-slip motion.

3 Okada Edge Dislocation Modeling

3.1 Methods

We model surface deformation due to slip on normal faults using Okada edge dislocations (Okada, 1985), using the *dmodels* Matlab package (modified for ease of use with our data formats) from Battaglia et al. (2013). As shown in Figure 5, the basic 2D model is a plane of infinite length (extending into the page), parameterized by the dip direction and angle (θ), and depths to the top and bottom edges (d_t and d_b, respectively), contained within an elastic half-space. In our approach, X is the lateral distance between the midline at x=0 and the top edge of the fault, and s is the magnitude of slip in the down-dip direction. This 2D analytical model of surface deformation consists of only two components: vertical and fault-perpendicular horizontal. When extended to the 3D analytic model, the edge dislocation is a plane of finite length (L) and the surface deformation includes vertical, eastward, and northward components of

motion. Due to the limitations of polar orbital paths, InSAR is insensitive to northward motion, and we exclude this component from our modeling.

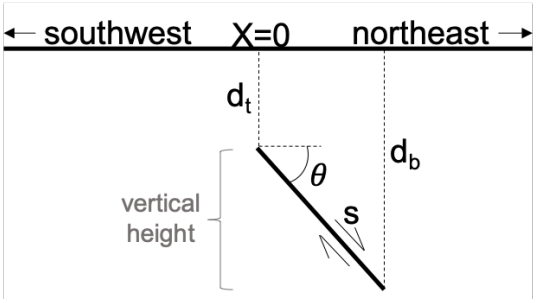

Figure 5. Schematic diagram of the fault geometry for a 2D edge dislocation in a homogeneous elastic half-space. In 3D, the predicted fault strikes northwest, thus the fault-perpendicular profile is in the northeast-southwest direction. Fault parameters are described in Table 2.

3.1.1 2D Modeling

We use the 2D model to constrain the approximate depth intervals of slip by comparing forward models of Okada edge dislocations to the measured InSAR data using a parametric sweep. Our initial assumption is that the linear feature of interest can be explained by a single infinitely long fault plane oriented parallel to the midline in Figure 4a and 4b. However, the study area undoubtedly consists of multiple deformation sources in addition to a single slipping fault which dominates the signal. In order to reduce the sensitivity of our analysis to these other sources, we created an average InSAR profile parallel to the solid gray line in Figure 4a and 4b, using data from within the red boxes. The resulting profiles are shown in Figure 4c and 4d. In c, the vertical profile is the black line; however, in d, the average east-west displacement depicted by the dashed black line is not strictly fault-perpendicular, as required in the data for the 2D modeling. It is not possible to determine the true northeast-southwest deformation from only two InSAR components; however, if we assume that the measured displacements along the linear feature are due to pure dip-slip motion on a fault parallel to the midline, then there is a unique solution to the required northeast-southwest displacements (H_{ne-sw}) via the trigonometric relationship in Equation 2:

$$H_{ne-sw} = \frac{H_{e-w}}{\cos\varphi}, \qquad (2)$$

where H signifies horizontal motion and subscript e-w indicates east-west motion. Variable φ is the angle between North and the strike of the midline (36°), as shown in Figure 4b. The resulting fault-perpendicular displacement profile is the solid black line in Figure 4d. In our model, we use the vertical and estimated northeast-southwest horizontal profiles as the reference data for misfit assessment within the gray regions in Figure 4c and 4d. The chosen regions in each profile have the same number of measurements (n), but are offset from each other, such that the area in vertical is centered around the valley at 150 m and in horizontal is centered around the peak at −605 m. Beyond these regions, the InSAR profiles deviate from the expected deformation due to a single edge dislocation and are more likely to be influenced by other sources.

In the parametric sweep, we assess the fit of all forward Okada edge dislocation models characterized by the parameter sets developed from the values listed in Table 2. We selected a common value for the Poisson ratio (0.25) and used the P velocity (4.3 km/s) from Sheng et al. (2020/submitted) to estimate a shear modulus of 15 GPa, keeping both parameters constant during modeling to simplify the parameter space. We determine the X-location for the top edge of the fault relative to the midline (x=0) directly from the model: for a given parameter set i consisting of d_t, d_b, θ, and dip direction, we compute the vertical forward model of the dislocation with the top edge at x=0 and 10 cm of normal slip, and then adopt the lateral offset between the minima in the vertical forward model and InSAR profile as the appropriate X-location.

With the full geometry for parameter set i defined, we determine the magnitude of slip (s) best-fitting the InSAR profiles by minimizing a modified RMS error (E), which we refer to as misfit, as defined in Equation 3:

$$E_i = \sqrt{\frac{\sum_{i=1}^{n}\left((\hat{v}_i-(v_i+DS_{v_i}))/2\right)^2+\left(\widehat{h_i}-(h_i+DS_{h_i})\right)^2}{2n}}. \quad (3)$$

Here, $\hat{v}$ and $\hat{h}$ are the vertical and horizontal displacements, respectively, from the forward model, the un-hatted v and h are from the InSAR profiles, and n is the number of samples in the InSAR profile, within the misfit assessment bounds. Since our main goal in the 2D modeling is to fit the wavelength and relative amplitudes of the vertical and horizontal data, we allow datum

389 shifts in each (DS_v and DS_h, respectively) during measurement of the misfit, such that the minima
390 in vertical and maxima in horizontal between the forward model and data are equal (see Figure
391 S6). We also weight the vertical differences by ½ in order to account for the higher amplitude in
392 vertical motion compared to horizontal and better allow the latter to influence the solution. We
393 prefer this weighted misfit assessment because a dip-slip edge dislocation results in vertical
394 displacements that are approximately twice the amplitude of the horizontal, within our chosen
395 misfit bounds, which is also the proportion observed in the InSAR profiles. Weighting the
396 vertical differences between data and model by ½ results in a solution in which the proportion of
397 differences to amplitude in each displacement component are comparable.

Parameter	**Values**	**Notes**
Dip Direction	northeast or southwest	Strike parallel to midline (dashed line in Figure 4a and 4b)
Dip Magnitude (θ)	5 - 90 (°)	θ is an integer
Depth to Top Edge (d_t)	100, 200, …, 6300 (m)	
Depth to Bottom Edge (d_b)	200, 300, …, 6400 (m)	$100\ m \leq (d_b - d_t) \leq 6300\ m$
Location of Top Edge (X)	--------	Determined from vertical model and InSAR
Shear Modulus (μ)	10 GPa	Kept constant
Poisson Ratio (υ)	0.25	Kept constant

398 **Table 2.** Parameter space for 2D edge dislocation models. We invert for slip magnitude (s) for
399 each parameter combination by minimizing misfit error E (Equation 3), and compare models
400 based on this misfit.

401 3.1.2 3D Modeling

402 While the 2D modeling is useful for constraining appropriate edge dislocation
403 parameters, we require the 3D model to analyze the relationship of proposed faults to the local
404 seismicity and well locations, and better understand the deformation due to slipping faults in the
405 context of the InSAR displacements in the full study area. Using the *dmodels* package (Battaglia

et al., 2013), we are able to extend any of the 2D, one-fault forward models to the full 3D space by adopting the *X*-location and uniform slip magnitude resulting from 2D modeling, and assigning finite length *L* (equal to the length of the midline) and strike direction (parallel to the midline). Observations from comparing these 3D, one-fault models to the full InSAR data inform our development of increasingly complex multi-fault models.

In the first stage of multi-fault modeling, we assume uniform slip on numerous edge dislocations of varying length. After selecting the number of faults (*N*) to include in the modeling, we manually select the endpoints of the top edge of each, thus defining their locations in the 3D space. For simplicity, we then select and assign identical d_t, d_b, and θ to each fault plane, but permit the strikes (as determined by the endpoints) and dip direction to vary on each, noting that we do not allow significant deviations ($\pm 10°$) from the strike of the midline or linear trends created by the moment tensor solutions from Sheng et al. (2020/submitted). We then solve for the magnitude of uniform slip on each fault plane using the relationship in Equation 4:

$$Wd = WGs', \quad (4)$$

where *d* is a vector of vertical and east-west horizontal InSAR data, s' is the unknown [*N* x 1] vector of slip magnitude on each fault plane, and *G* is the Green's function matrix relating slip magnitude to vertical and east-west horizontal surface deformation at each pixel, via the Okada (1985) equations. Matrix *W* is a diagonal weighting matrix that prioritizes data pixels near the fault segments. Along its diagonal is $1/R_i^2$, where R_i is the distance between data pixel *i* and the top edge of the nearest fault segment. We use *dmodels* (Battaglia et al., 2013) to generate the appropriate *G* matrix and apply Equation 4 to find the vector s' of uniform dip-slip magnitudes that best fits the selected InSAR data in a least-squares sense.

After developing a uniform-slip, multi-fault model, we introduce additional complexity by discretizing each plane into finite patches approximately 1000 m in length along strike and 200 m in down-dip width. The slip vector s' is now equal in length to the number of discretized patches. Equation 4 is significantly underdetermined, leading to an unrealistically rough solution of vector s'. Therefore, for the patch model we include a smoothing operator that minimizes the

2D second-derivative of fault slip, resulting in the regularized inversion relation shown in Equation 5:

$$\begin{bmatrix} Wd \\ \mathbf{0} \end{bmatrix} = \begin{bmatrix} WG \\ \alpha^2 D \end{bmatrix} s', \quad (5)$$

where α is the Lagrange operator that determines the weight put on the smoothing, and D is the second-order finite difference operator such that $\nabla^2 s' = Ds'$.

3.2 Results

3.2.1 2D Modeling

The purpose of the 2D, one-fault modeling was to constrain the approximate depth intervals (d_t *to* d_b) of slip. As indicated in Table 2, we explored vertical slip heights (d_b-d_t) ranging from 100 m - 6300 m, contained between depths of 100 m - 6400 m. The chosen range of d_t and d_b approximately corresponds to the complete geologic section above the basement (Figure 1c). In our simple 2D model there are parameter trade-offs, in which some parameter sets are geologically more realistic than others, despite having similar misfit to the InSAR data. To explore these trade-offs, we condensed our parameter space to include fault width ($w = (d_b - d_t)/\sin\theta$), the approximate 2D stress drop ($\Delta\sigma_{2D} = 0.85\mu s/w$) (Starr, 1928; Kanamori & Anderson, 1975), and the midpoint depth of the dislocation.

In Figure S4, we show the trade-offs between stress drop and fault width for subsets of southwest-dipping faults with vertical heights ranging between 100-1500 m, colored by the midpoint depth range. All subsets display similar trends (e.g. greater fault widths and shallower depths require lower stress drops to fit the data). Additionally, for vertical height subsets between 100-1000 m, the misfit values of the best 20% of models are virtually indistinguishable, although a further increase in vertical height gradually increases the misfit (Figure S5). Despite fitting the InSAR data, most stress drops for models with vertical heights of 100 m exceed 100 MPa, which is unrealistically high. For vertical heights of 500 m, the stress drops reduce to <35 MPa, and for vertical heights of 1500 m, all explored models have stress drops <4 MPa. Although a further increase in vertical height reduces the predicted stress drops, the misfit values of the best-fitting models increase to unacceptably high levels (Figure S5). We thus constrain our parameter space

460 to include only those models with vertical heights ranging between 500-1500 m, to maintain a
461 balance between plausible stress drops and model fit.

462 In addition to highlighting important trade-offs, Figure S4 shows that, in all subsets of
463 vertical height, the best-fitting models have midpoint depths around 2200 m, regardless of fault
464 width. While the best-fitting midpoint depth appears to be invariant to vertical heights and width,
465 the midpoint depth also has low sensitivity to dip angle. In Figure 6, we show model subsets with
466 vertical heights of 500 m (left) and 1500 m (right), and with either southwest- or northeast-dip
467 (top and bottom panels, respectively). The model misfit is shown as a function of midpoint depth
468 and dip angle. Depending on the vertical height, the best 20% of models in each dip bin have
469 mean depths between 2100 m – 2400 m. These depths coincide with the Delaware Mountain
470 Group, the formation in which wastewater disposal is concentrated and the majority of the
471 earthquakes occur, suggesting a connection between fluid injection and fault movement.

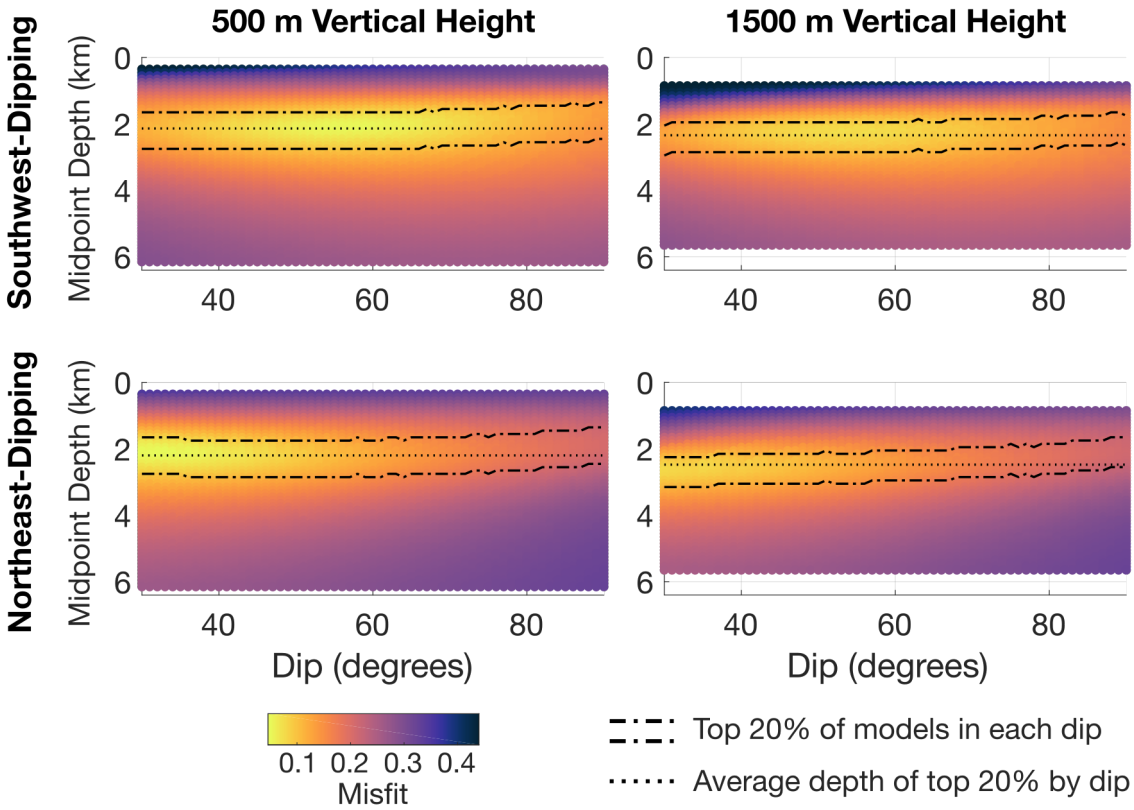

472

473 **Figure 6.** Misfit values for models as a function of midpoint depth, dip magnitude and direction,
474 and vertical height. Regardless of parameter set, the top 20% of models in each integer dip bin

have midpoints between ~1.5 km to ~3 km. We exclude dips below 30° based on the local stress conditions (see Figure 7).

We are able to constrain the depth intervals and vertical heights from misfit assessment and geomechanical arguments about stress drop. We can do a similar exercise to constrain the expected dip magnitudes. Table 1 lists the high-angle moment tensor solutions from Sheng et al. (2020/submitted), which have a median dip of 70°. For each earthquake, there exists an auxiliary low-angle plane; these low-angle planes have a median dip of 22°. Although the moment tensor analysis alone cannot distinguish between the two dips, we can eliminate the low-angle dips based on the local stress conditions. In a predominantly normal-faulting stress regime, as is the case in the Delaware Basin (Lund Snee and Zoback, 2018), low-angle faults are the furthest from failure. Figure 7 shows **a**, the Mohr circle derived from measurements of the principal stress components in the southern Delaware Basin from Dvory and Zoback (2021), and **b**, the minimum increase in pore pressure (dP) required for fault failure as a function of dip. Not only are low-angle faults the least likely to slip, faults with dips <30° are precluded from slipping by the local stress conditions, since the change in pore pressure required would exceed the fracking threshold (dashed line in Figure 7b) and create microfractures in lieu of fault-reactivation. Therefore, we expect to see active high-angle faults with dips >60°, consistent with the high-angle fault planes from the moment tensor solutions (Table 1).

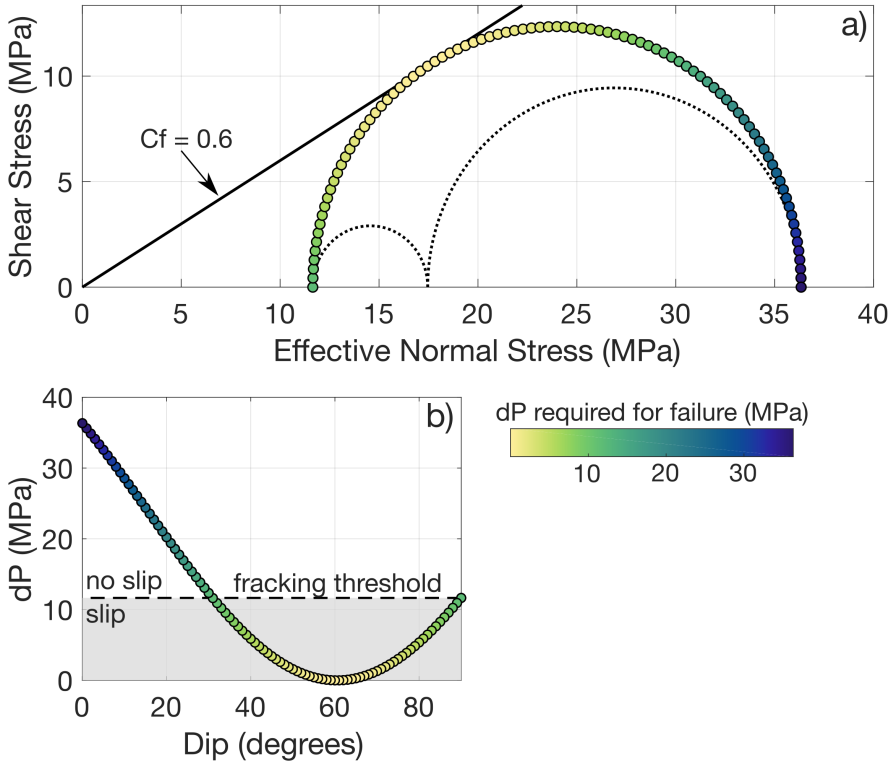

493

494 **Figure 7.** Minimum change in pore pressure (dP) required to reactive faults of specified dip. **a**
495 Mohr circle and relative stresses for the Delaware Mountain Group (Dvory and Zoback, 2021),
496 assuming a coefficient of friction (Cf) of. 0.6. **b** minimum dP for slip as a function of dip. Any
497 dP exceeding the fracking-threshold (dashed line in b) will produce new microfractures,
498 significantly reducing the local effective stress. Thus, faults with orientations of dP > fracking-
499 threshold are not expected to slip.

500 Figure 6 shows that the best-fitting one-fault models in our constrained parameter space
501 have dips between 30°-40° (northwest-dipping) or 50°-60° (southwest-dipping), suggesting that
502 the southwest-dipping faults fit the InSAR data better under the constraint of high-angle dips.
503 However, it is important to highlight that we allow a datum shift of the InSAR data during the
504 misfit assessment, as demonstrated in Figure S6, which compares the 2D forward models of the
505 best-fitting southwest- and northeast-dipping edge dislocations with dips of 75° and vertical
506 heights of 1000 m (see Table S1 for other parameters). The southwest-dipping fault does indeed
507 fit the datum-shifted InSAR profiles better than the northeast-dipping example. In contrast, we
508 note that the horizontal InSAR profile as measured (i.e. no datum shift) is better represented by

the northeast-dipping fault, though there is a sacrifice in vertical fit. These results suggest an ambiguity in the dip direction for a single fault that truly best fits the InSAR data.

3.2.2 3D Modeling

The next step is to consider slip models of finite length and uniform slip in the full 3D space. Figure S7 depicts the 3D finite-fault model for each 2D model from Figure S6. Both models reasonably reproduce the vertical subsidence along the linear deformation feature of interest, albeit with lower magnitude than the InSAR observations. In the east-west horizontal component, however, the northwest end of the midline in the InSAR data appears to be dominated by a southwest-dipping fault, whereas the southeast end may be dominated by slip on a northeast dipping fault. Therefore, we explore the possibility of a two-fault model consisting of a combination of the oppositely-dipping single-fault models from Figure S7. Using these observations and the expected slip interval depths constrained from the 2D model, we develop a model with two high-angle finite edge dislocations dipping toward each other in a graben structure, each with uniform slip, determined using Equation 4 (Figure S8). The southwest-dipping fault is rather short, but its extension along strike would contain the Group 1 earthquakes from Table 1, suggesting that the fault plane may be much longer, despite slip being concentrated in an isolated section. We thus extend each fault plane along its strike and discretize each into multiple patches. We also include a small northeast-dipping fault parallel to the Group 2 earthquakes from Table 1. Using the regularized solution described in Equation 5, we solve for the dip slip magnitude on each patch of the three defined faults, using $\alpha = 50$ due to its position on the bend of the L-curve of the solution semi-norm vs. residual norm logscale plot (Figure S9).

We compare the forward model of vertical and east-west horizontal surface displacements from the patched, three-fault model to the measured InSAR data in Figure 8. The top edge of each fault (F1 – F3) is marked by a solid red line and its downward-looking extent is outlined by the dotted black line. The slip distributions along each fault are shown in Figure 9, where (a) depicts the bird's eye view of the average slip along each fault's down-dip direction, and (b-d) display the side-view of each fault from the perspective of the arrow in Figure 9a. In Figure 9c-9d, we also include the along-strike profile of modeled (black line) and InSAR (red line) surface deformation directly above the top edge of traces F2 and F3, which flank the linear

deformation feature of interest. In Figures 8 and 9a, we include the locations of earthquakes from Table 1, which highlight that Group 1 falls along the trace of F3, and Group 2 aligns with F1. Therefore, in Figure 9b-9d, we show only the earthquake locations in the side-view plots for the faults with which they are associated (Group 1 in Figure 9d and Group 2 in 9b). The final detail in Figure 9 is the location of active disposal wells (gray dots), which are labeled by the volume of injected fluid in millions of barrels (MMbbl) during the time span of our study. In Figure 9b-9d, we include only the disposal wells within 2 km of the fault planes. The perforation interval of each well is indicated by the solid black lines.

The main linear deformation feature in vertical (Figure 8a) is reproduced well in the forward model (Figure 8c); likewise, the horizontal deformation from the forward model (Figure 8d) agrees with the westward sense of motion flanking the linear feature in the InSAR data (Figure 8b), without requiring a datum shift. This model, however, cannot explain the two subsidence features to the southwest of F2, nor the uplift to the southeast of F3. Consequently, there are unmodeled displacement features in the horizontal component which coincide with the same geographical areas. In Figure 9c-9d, the comparison of the model and InSAR profiles also highlight some residual deformation that has not been captured by the model. These residuals are a direct result of our decision to favor smoothly varying slip models to prevent overfitting the data with unrealistic slip distributions.

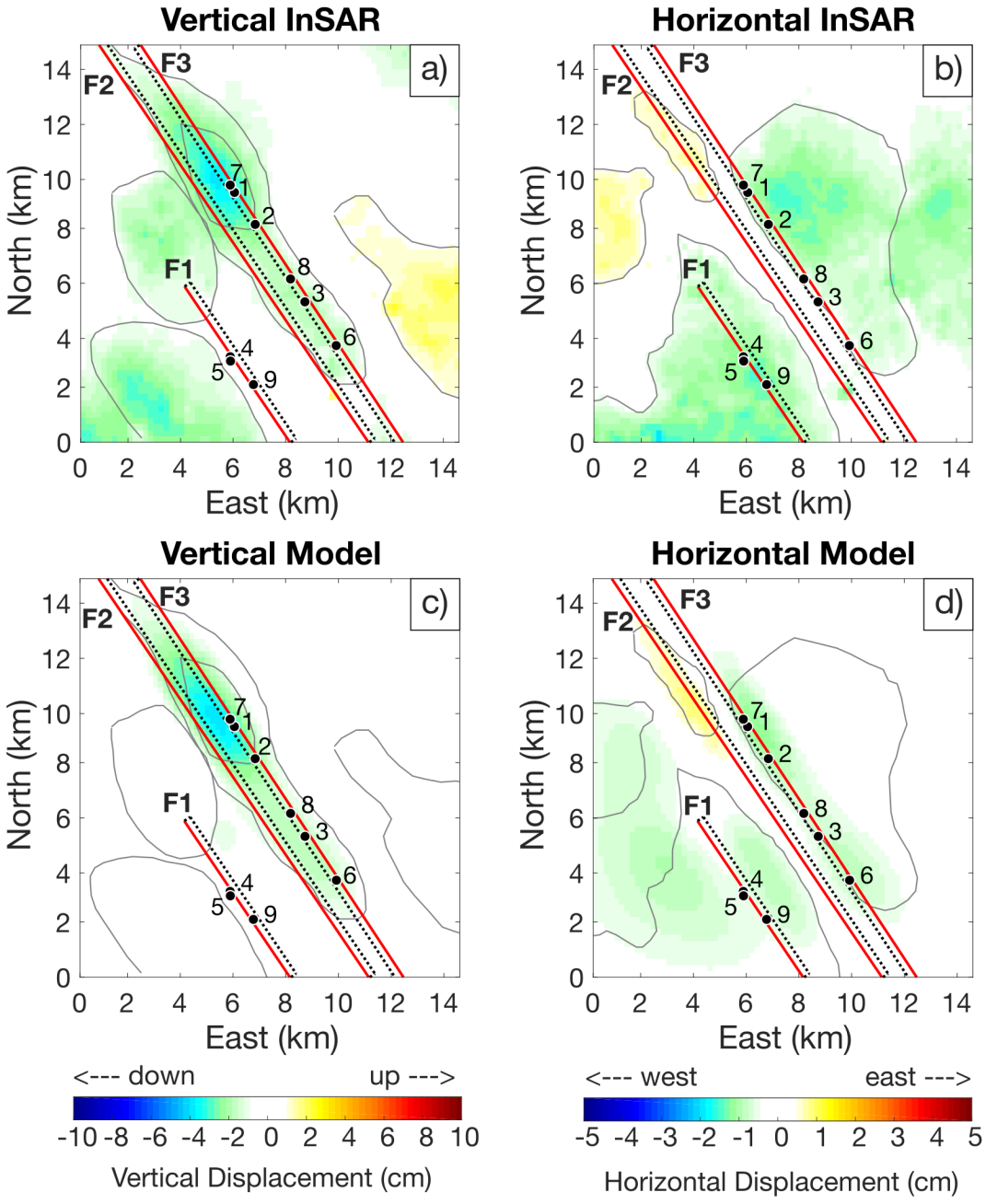

Figure 8. Three-fault model in a 3D space. The top panel is the original InSAR data, where **a** is vertical and **b** is horizontal, with major features outlined in gray in order to better compare with the forward model in the lower panel, with **c** the vertical forward model and **d** the horizontal forward model. The two edge dislocations are represented by the red lines (top edge of fault) with bird's-eye extent depicted by the dotted lines.

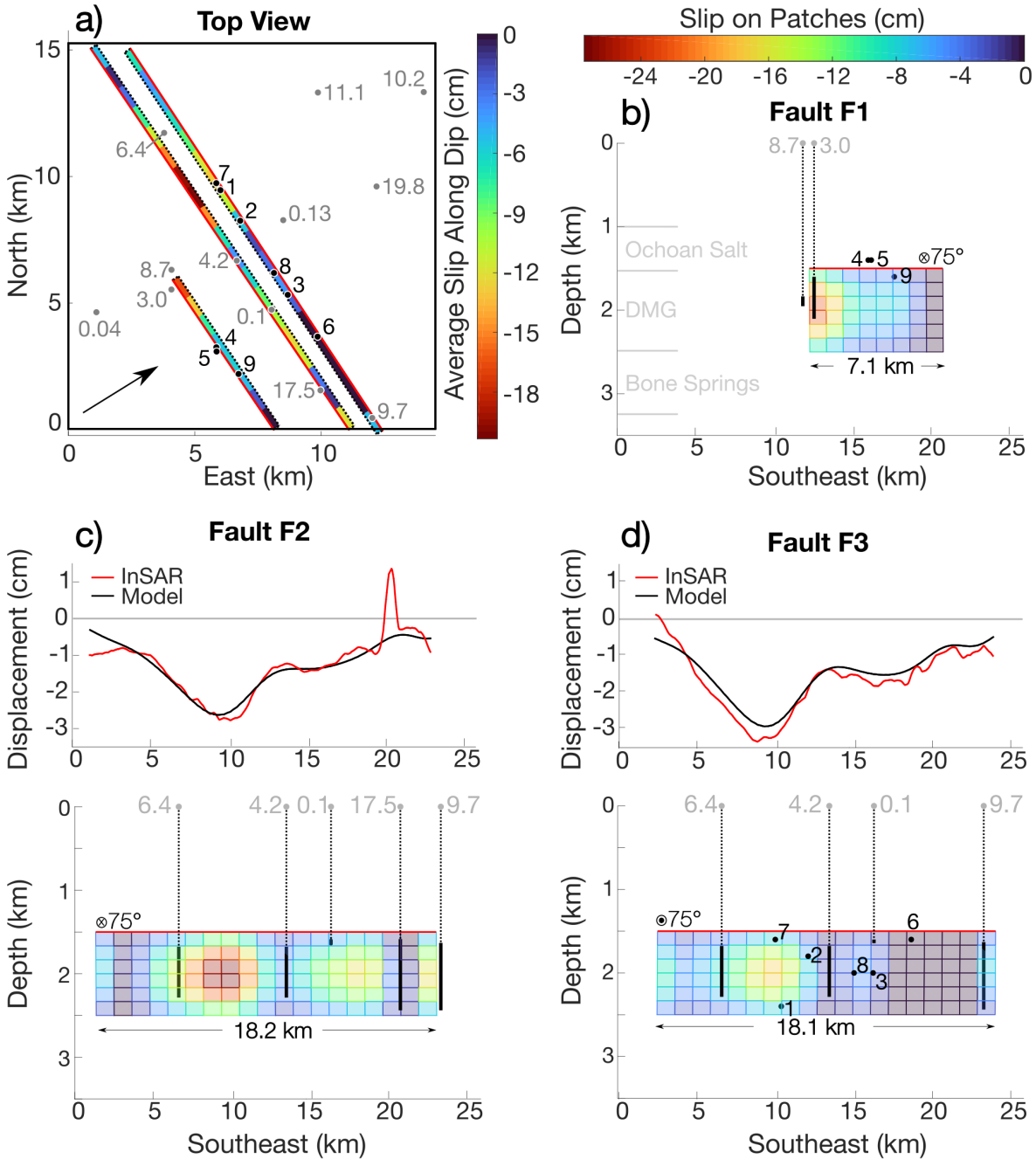

Figure 9. Slip distribution on the three-fault edge dislocation model. The top view in **a** shows the spatial relationship of the faults with the earthquake moment tensors (black dots) and disposal wells (gray dots). The numbers that accompany disposal wells are the values of cumulative injection volume between March 2015-March 2020, in millions of barrels (MMbbl). Plots **b-d** show the side view of each fault from the perspective of the black arrow in **a**. Faults F2 and F3 (**c** and **d**, respectively) also display the InSAR and model surface deformation directly above the

569 top edge of each respective fault. Earthquake moment tensors and disposal wells within 2 km of
570 each fault are included in **b-d**. Formation intervals are also indicated on the cross-sectional
571 profiles in **b**.

572 The maximum amount of slip along F1 is mostly to the northwest of the Group 2
573 earthquakes, all of which have a northeast dip, agreeing with the dip of F1 (Figure 9a and 9b).
574 Although there are no large earthquakes that spatially locate along the trace of F2, this fault has
575 the greatest displacement (27.5 cm) and greatest extent of slip, as shown in Figure 9a and 9c. The
576 majority of slip along F3 is confined to the north of earthquakes #2, #7, and #1, and there is a
577 small amount of slip (~6 cm) near earthquakes #8 and #3. We note, however, that the dip for
578 earthquakes #6 and #7 are northeast, suggesting that they may belong to F2 or an additional
579 unmodeled fault within the graben structure. In the former case, both northeast-dipping
580 earthquakes would locate above the two local slip maxima on F2, whereas the latter case requires
581 further modeling to draw any conclusions regarding the relationship to slip. The largest
582 earthquakes do not collocate with the patches hosting the greatest predicted slip magnitudes,
583 suggesting that the faults are principally slipping aseismically. Additional evidence stems from
584 the timing of earthquakes #6-9, which all occurred after the end of the InSAR study period (post-
585 March, 2020). Thus, the observed slip only has the potential to be attributed to earthquakes #1-5,
586 which have a peripheral relation to the greatest slip magnitudes.

587 While the majority of proposed slip cannot be attributed to the earthquakes, the regions of
588 large slip along each fault trace do coincide with the location of disposal wells. In Figure 9b-9d,
589 local areas of maximum slip lie between adjacent disposal wells. For instance, the patches of
590 maximum slip on F2 lie between wells with disposal volumes of 6.4 and 17.5 MMbbl, with the
591 absolute maximum falling directly between wells with 6.4 and 4.2 MMbbl. Even on F3, where
592 the maximum slip also lies adjacent to the well with 6.4 MMbbl, there is an observable increase
593 in slip at the right edge of the fault that coincides with the well with 9.7 MMbbl of injection
594 volume. Consequently, there is evidence for a link between fault slip and fluid injection in our
595 study area.

596 Although the spatial relationship between fault slip and disposal is clear, there does not
597 appear to be a direct correlation between the amount of slip and disposal volumes. However,

598 there are many other variables to consider, including disposal rate, distance from the fault, and
599 hydraulic and frictional properties of the fault. We note that the vertical InSAR profile along F2
600 (Figure 9c) shows signs of uplift directly above the disposal wells with the largest injection
601 volumes, suggesting that the measured deformation may be due to the combination of many
602 effects. In this case, it appears that injection-related uplift is superimposed on the subsidence
603 signal from fault slip. The combined effects pose a challenge for isolating the true magnitude of
604 slip on each fault patch. For example, on fault F2 near the disposal well with 17.5 MMbbl
605 injection volume, there is a distinct column of little fault motion interrupting an otherwise
606 smooth slip distribution on either side. It is possible that uplift related to the injection wells is
607 causing an underestimation of the slip magnitudes, at this location and near other disposal wells
608 along the fault traces.

609 **4 Discussion**

610 Our 2D and 3D edge dislocation model results show that the observed InSAR surface
611 deformation can in part be explained by slip on high-angle normal faults within the DMG, with
612 possible extension into the overlying Ochoan salts and underlying Bone Springs. In our small
613 study area, our model consists of a long, shallow graben structure, and at least one other fault
614 plane approximately 3-4 km to the southwest of the graben. Although there have been no
615 detailed structural analyses in our study area, recent studies using 3D seismic arrays have
616 mapped similar graben structures throughout Reeve's county (Charzynski, et al., 2019; Hennings
617 et al., 2021). All occurrences show graben structures mainly spanning the DMG, with slight
618 extension into the Ochoan and Bone Springs. The grabens are all high-angle, ~0.25-1 km wide
619 (as measured by their top edges), and spaced 2-4 km apart. The three-fault model we developed
620 has identical characteristics, suggesting it is a part of this larger graben network.

621 The occurrence of deformation and the improved focal depth analysis from Sheng et al.
622 (2020/submitted) highlight that these shallow grabens are not only present, but also active. In
623 Figure 10, we have summarized the depth distribution of average slip (blue histogram), moment
624 tensor centroids (red histogram), and relocated earthquake hypocenters (gray histogram), along
625 with the 1D geological model Sheng et al. (2020/submitted) developed from the P-wave velocity
626 profile (black line). All data peak at a depth of ~2000 m in the middle of the DMG, which hosts

627 all the local wastewater disposal. Not only do these data fall within the same formation, they
628 have strong spatial relationships to one another. We were able to develop a discretized fault
629 model that aligns with the larger earthquakes in our study area and agrees with the moment
630 tensor solutions in terms of high-angle dip, as suggested by the local stress conditions, and sense
631 of predominantly dip-slip motion. Furthermore, though we did not constrain our model with the
632 available well data, wastewater disposal wells are located near patches of greatest slip on each
633 fault. Therefore, it seems likely that the nearby fluid injection is activating these normal faults;
634 however, the displacement is clearly not all seismic.

635 We calculate the cumulative geodetic moment along the patched surfaces of all three faults
636 F1-F3, using equations for seismic moment:

637 $$M_0 = \mu A S, \qquad (6)$$

638 where μ as the shear modulus, A is the rupture area, and S is the average slip. To convert seismic
639 moment to moment magnitude M_W, we use the definition from Hanks and Kanamori (1979) with
640 M_0 in Newton-meters:

641 $$M_W = \frac{2}{3}(log_{10}M_0 - 9.1). \qquad (7)$$

642 The combined equivalent magnitude released during slip on all patches is $M_W = 5.0$, whereas the
643 combined equivalent magnitude of all earthquakes recorded by the TexNet array (between 01-
644 01-2017 to 03-31-2020) in our study area is $M_W = 3.9$. Hence seismicity accounts for only ~2%
645 of the predicted fault slip. If normal slip is contributing to the InSAR observations, as suggested
646 by our model, it is predominantly aseismic.

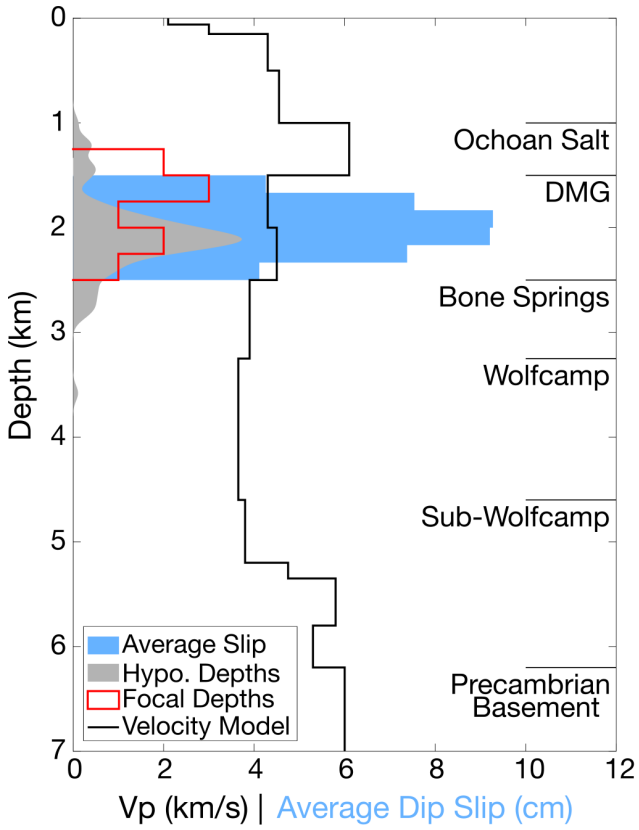

Figure 10. Summary of slip intervals from Okada modeling compared to the relocated earthquake depths (Hypo. Depths), moment tensor centroid depths (Focal Depths), and velocity model from Sheng et al. (2020/submitted). All fault motion (seismic and aseismic) extends through the Delaware Mountain Group (DMG), the main formation used for wastewater injection. Local formation intervals indicated.

To date, the role of aseismic slip in induced seismicity has been largely limited to indirect inference and associated with hydraulic fracturing (Cornet et al., 1997; Guglielmi et al., 2015; Eyre et al., 2019; Eyre et. al., 2020; Zhu et al., 2020), so the implications of its occurrence in the Delaware Basin are challenging to know. Though Sheng et al. (2020/submitted) and our work suggest that wastewater disposal is likely inducing seismic and aseismic slip on normal faults in the DMG it is unclear whether both are a direct consequence of the fluid injection, or whether aseismic slip triggers seismic events and/or vice versa. Based solely on our static 3D model, it is clear that the largest earthquakes along F1 and F3 do not coincide with the patches hosting the largest cumulative displacements (up to 27.5 cm), but rather are located around the periphery in

patches with slip < 10 cm. This suggests that hydraulic and frictional conditions vary along the faults.

Although our focus here has been on a small area in the Delaware Basin, we can extend our findings to the rest of the basin, which has contrasting deformation and seismicity patterns between the southern and northern sections. As demonstrated in the full-basin InSAR results (Figure 2), the linear deformation features only occur where there is seismic activity, suggesting that aseismic and seismic slip are intimately linked. Thus, the lack of seismicity and linear deformation features to the north of the Grisham fault could indicate that favorably oriented normal faults in the DMG are absent. However, this explanation lacks supporting evidence and is rather ad hoc. Dvory and Zoback (2021) analyzed the stress state and frictional stability of faults in the basin. They found that the fluid pressure in the DMG in the northern portion of the basin was diminished by conventional oil and gas production in that formation in the decades before unconventional exploitation began. Under this explanation, pressures are currently too low to induce fault slip, even under conditions of wastewater injection in the presence of favorably oriented faults. In contrast, the stress state is near-critical south of the Grisham fault, where very little production has occurred in the DMG. Modest pressure rise of a few MPa due to wastewater disposal in the DMG would bring favorably-oriented normal faults to failure, both seismically and aseismically.

It is essential to highlight the importance of including both InSAR components in the development of our model. The observations we made about the east-west horizontal deformation patterns produced from the single faults in Figure S7 directly guided us to the two-fault graben structure in Figure S8. In addition, faults F1 and F3, which we in part defined to align with the focal depths and sense of slip of the nine larger earthquakes, cannot reproduce the observed InSAR deformation without the inclusion of fault F2. Had we used only the vertical deformation in the development of our model, we would have lacked the information needed to determine the geometry of all three faults, which altogether create a consistent story with the additional geophysical data available and recent works showing shallow graben structures in the DMG (Charzynski, et al., 2019; Hennings et al., 2021).

690 One limitation of our model is the assumption that the observed surface deformation is
691 due exclusively to fault slip. More likely it results from the combined effects of fault slip (both
692 seismic and aseismic), oil and gas production, wastewater and CO_2 injection, and groundwater
693 pumping for municipal, agricultural, and industrial purposes. Further evidence for multiple
694 causes is clearer in the northern portion of the basin where there is observable deformation but
695 no obvious patterns suggestive of fault movement. As Figure 9c and 9d show, the smoothed slip
696 model has up to 2 cm of misfit to the InSAR data, suggesting additional mechanisms contribute
697 to the surface displacement. In particular, there is less subsidence in the InSAR data than
698 predicted near some disposal wells, suggesting uplift from fluid injection. If the latter contributes
699 to surface deformation, then we cannot rule out production-related subsidence as well, especially
700 from shallow groundwater wells. Staniewicz et al. (2020) addressed the possibility of multiple
701 deformation sources by removing the predicted vertical deformation from normal fault motion
702 and computing residual vertical displacements resulting from subsurface volume changes. While
703 forming a useful approach for modeling volumetric changes from fluid extraction and injection,
704 including these in our model would not change our primary conclusion that high-angle normal
705 faults in the DMG are moving.

706 **5 Conclusions**

707 Our InSAR analysis shows a stark contrast in deformation patterns between the northern
708 and southeastern portions of the Delaware Basin. The three-fault model we developed from both
709 components of these InSAR data suggests that fault motion is responsible for the linear
710 deformation features in the southeastern portion of the Delaware Basin. Based on the spatial
711 relationship between wastewater disposal wells, critically stressed faults, and relocated
712 earthquakes, we have shown that wastewater injection in the DMG has likely been inducing both
713 aseismic and seismic fault movement in this area. However, it remains unclear whether the
714 aseismic slip and seismic events are both a direct result of pore pressure increase, or if induced
715 aseismic slip triggers the seismicity or vice versa. Theoretical numerical modeling of injection-
716 induced aseismic slip will be paramount to understanding the complex subsurface response to
717 wastewater disposal, and our work provides observation-based slip models that can be used to
718 constrain and contextualize these efforts. As we continue to explore the evidence for aseismic
719 slip in the rest of the southern Delaware Basin and determine the likely geomechanical

720 mechanisms contributing to deformation in the northern portion of the basin, it may be possible
721 to constrain the conditions that lead to aseismic and seismic slip, so operators can better plan the
722 location and operating standards for future wells.

723 **Acknowledgements and Data Availability Statement**

724 This work was supported by the Stanford Center for Induced and Triggered Seismicity (SCITS)
725 and the Department of Energy (Basic Energy Sciences; Award DE-SC0020445). The authors
726 report no conflicts of interest pertaining to this work.

727 The InSAR cumulative displacements (vertical and east-west horizontal) are available in data
728 citation: Pepin et al. (2021) via https://doi.org/10.5281/zenodo.5348368. The edge dislocation
729 modeling software we used for this research is available in Battaglia et al. (2013) via download
730 at https://pubs.usgs.gov/tm/13/b1/. The InSAR single-look-complex images for all orbits are
731 available in: ASF DAAC (2014-2020). Users must register for a free Vertex account to access
732 data. The TexNet data and station information are available in this in-text citation reference:
733 Savvaidis et al., 2019. The USGS Earthquake Catalog can be found in U.S. Geological Survey,
734 Earthquakes Hazard Program (2017). Relocated earthquakes and moment tensor solutions are
735 available in Sheng et al. (2020/submitted). The industry well data supporting this research are
736 available via Enverus' (previously Drillinginfo) online database (Enverus, 1999). This database
737 requires a paid subscription and is not available to the general public. Groundwater well data
738 supporting this research is available for free via the Texas Water Development Board in their
739 Groundwater Database (GWDB) and Brackish Resource Aquifer Characterization System
740 (BRACS) Database via data citation: Texas Water Development Board (2013). The data on
741 stress orientations and local stress are included, respectively, in these papers: Lund Snee and
742 Zoback, 2018 and Dvory and Zoback, 2021.

743 **References**

744 ASF DAAC (2014-2020), contains modified Copernicus Sentinel data 2014-2020, processed by
745 ESA. *Vertex Data Search*. Retrieved from https://search.asf.alaska.edu/#/. Accessed
746 2020-07-01.

747 Battaglia, M., Cervelli, P. F., & Murray, J. R. (2013). A MATLAB software package for
748 modeling curstal deformation near active faults and volcanic centers. *Journal of*
749 *Volcanology and Geothermal Research, 254*, 1-4. https://pubs.usgs.gov/tm/13/b1/.

750 Berardino, P., Fornaro, G., Lanari, R., & Sansosti, E. (2002). A New Algorithm for Surface
751 Deformation Monitoring Based on Small Baseline Differential SAR Interferograms.
752 *IEEE Transactions on Geoscience and Remote Sensing, 40*(11), 2375-2383. doi:
753 10.1109/TGRS.2002.803792.

754 Charzynski, K., Faith, K., Fenton, Z., Shedeed, A., McKee, M., Bjorlie, S., & Richardson, M.
755 (2019). Delaware Basin Horizontal Wolfcamp Case Study: Mitigating H2S and
756 Excessive Water Production through Isolating Densely Fractured Intervals Correlative to
757 Seismically Mapped Shallow Graben Features in the Delaware Mountain Group. *SEG*
758 *Global Meeting Abstracts*, (pp. 4126-4141).

759 Chen, C. W., & Zebker, H. A. (2001). Two-dimensional phase unwrapping with use of statistical
760 models for cost functions in nonlinear optimization. *Journal of the Optical Society of*
761 *America, 18*(2), 338-351.

762 Cornet, F. H., Helm, J., Poitrenaud, H., & Etchecopar, A. (1997). Seismic and Aseismic Slips
763 Induced by Large-scale Fluid Injections. In S. Talebi, *Seismicity Associated with Mines,*
764 *Reservoirs and Fluid Injections* (Vols. https://doi-org.stanford.idm.oclc.org/10.1007/978-
765 3-0348-8814-1_12, pp. 563-583). Birkhäuser, Basel: Pageoph Topical Volumes.

766 Deng, F., Dixon, T., & Xie, S. (2020). Surface Deformation and Induced Seismicity Due to Fluid
767 Injection and Oil and Gas Extraction in Western Texas. *Journal of Geophysical*
768 *Research: Solid Earth, 125*(5). https://doi.org/10.1029/2019JB018962.

769 Dvory, N. Z., & Zoback, M. D. (2021). Prior oil and gas production can limit the occurrence of
770 injection-induced seismicity: A case study in the Delaware Basin of western Texas and
771 southeastern New Mexico, USA. *Geology, 49*, XXX-XXX,
772 https://doi.org/10.1130/G49015.1.

773 Ellsworth, W. L. (2013). Injection-Induced Earthquakes. *Science, 341*(6142), 1225942. DOI:
774 10.1126/science.1225942.

775 Enverus (1999). *DrillingInfo Database*. Retrieved from Enverus: https://www.enverus.com/.
776 Accessed 2020-07-02.

777 Eyre, T. S., Eaton, D. W., Garagash, D. I., Zecevic, M., Venieri, M., Weir, R., & Lawton, D. C.
778 (2019). The role of aseismic slip in hydraulic fracturing-induced seismicity. *Sci. Adv.,*
779 *5*(eaav7172). DOI: 10.1126/sciadv.aav7172.

780 Eyre, T. S., Zecevic, M., Salvage, R. O., & Eaton, D. W. (2020). A Long-Lived Swarm of
781 Hydraulic Fracturing-Induced Seismicity Provides Evidence for Aseismic Slip. *Bull.*
782 *Seismol. Soc. Am., 110*, 2205-2215, doi: 10.1785/0120200107.

783 Farahbod, A. M., Kao, H., Cassidy, J. F., & Walker, D. (2015). How did hydraulic-fracturing
784 operations in the Horn River Basin change seismicity patterns in northeastern British
785 Columbia, Canada? *The Leading Edge, 34*(6), 658-663.
786 http://dx.doi.org/10.1190/tle34060658.1.

787 Frohlich, C., DeShon, H., Stump, B., Hayward, C., Hornbach, M., & Walter, J. I. (2016). A
788 Historical Review of Induced Earthquakes in Texas. *Seismological Research Letters,*
789 *87*(4), 1022-1038. doi: 10.1785/0220160016.

790 Frohlich, C., Ellsworth, W., Brown, W. A., Brunt, M., Luetgert, J., MacDonald, T., & Walter, S.
791 (2014). The 17 May 2012 M4.8 earthquake near Timpson, East Texas: An event possibly
792 triggered by fluid injection. *Journal of Geophysical Research: Solid Earth, 119*, 581-593,
793 doi:10.1002/2013JB010755.

794 Grandin, R., Vallée, M., & Lacassin, R. (2017). Rupture Process of the Mw 5.8 Pawnee,
795 Oklahoma, Earthquake from Sentinel-1 InSAR and Seismological Data. *Seismological*
796 *Research Letters, 88*(4), 994-1004, doi: 10.1785/0220160226.

797 Guglielmi, Y., Cappa, F., Avouac, J.-P., Henry, P., & Elsworth, D. (2015). Seismicity triggered
798 by fluid injection-induced aseismic slip. *Science*, 1224-1226. DOI:
799 10.1126/science.aab0476.

800 Hanks, T. C., & Kanamori, H. (1979). A Moment Magnitude Scale. *Journal of Geophysical*
801 *Rsearch, 84*(B5), 2348-2350.

802 Hennings, P., Dvory, N., Horne, E., Li, P., Savvaidis, A., & Zoback, M. (2021). Stability of the
803 Fault Systems That Host-Induced Earthquakes in the Delaware Basin of West Texas and
804 Southeast New Mexico. *The Seismic Record, 1*(2), 96-106, doi: 10.1785/0320210020.

805 Hornbach, M. J., DeShon, H. R., Ellsworth, W. L., Stump, B. W., Hayward, C., Frohlich, C., . . .
806 Luetgert, J. H. (2015). Causal factors for seismicity near Azle, Texas. *Nature*
807 *Communications, 6*(6728), DOI: 10.1038/ncomms7728.

808 Kanamori, H., & Anderson, D. L. (1975). Theoretical Basis of Some Empirical relations in
809 Seismology. *Bulletin of the Seismological Society of America, 65*(5), 1073-1095.

810 Keranen, K. M., Savage, H. M., Abers, G. A., & Cochran, E. S. (2013). Potentially induced
811 earthquakes in Oklahoma, USA: Links between wastewater injection and the 2011 Mw
812 5.7 earthquake sequence. *Geology, 41*(6), 699-702. doi:10.1130/G34045.1.

813 Kim, J.-W., & Lu, Z. (2018). Association between localized geohazards in West Texas and
814 human activities, recognized by Sentinel-1A/B satellite radar imagery. *Scientific Reports,*
815 *8*(4727). DOI:10.1038/s41598-018-23143-6.

816 Kim, J.-W., Lu, Z., & Kaufmann, J. (2019). Evolution of sinkholes over Wink, Texas, observed
817 by high-resolution optical and SAR imagery. *Remote Sensing of Environment, 222*, 119-
818 132. doi:https://doi.org/10.1016/j.rse.2018.12.028.

819 Kovach, R. L. (1974). Source Mechanisms for Wilmington Oil Field, California, Subsidence
820 Earthquakes. *Bulletin of the Seismological Society of America, 64*(3), 699-711.

821 Lomax, A., & Savvaidis, A. (2019). Improving Absolute Earthquake Location in West Texas
822 Using Probabilistic, Proxy Ground-Truth Station Corrections. *Journal of Geophysical*
823 *Research: Solid Earth, 124*(11), 447-11,465. https://doi.org/10.1029/ 2019JB017727.

824 Lund Snee, J.-E., & Zoback, M. D. (2018). State of stress in the Permian Basin, Texas and New
825 Mexico: Implications for induced seismicity. *The Leading Edge*, 127-134.
826 https://doi.org/10.1190/tle37020127.1.

827 Massonnet, D., & Feigl, K. L. (1995). Satellite radar interferometric map of the coseismic
828 deformation field of the M = 6.1 Eureka Valley, California Earthquake of May 17, 1993.
829 *Geophysical Research Letters, 22*(12), 1541-1544.

830 Okada, Y. (1985). Surface Deformation Due to Shear and Tensile Faults in a Half-Space.
831 *Bulletin of the Seismological Society of America, 75*(4), 1135-1154.
832 https://doi.org/10.1785/BSSA0750041135.

833 Pepin, K.S., Ellsworth, W.L., Sheng, Y., Zebker, H. (2021). InSAR Displacements in the
834 Delaware Basin, TX (Version 1) [Data set]. Zenodo.
835 https://doi.org/10.5281/zenodo.5348368.
836
837 Pepin, K. S., Zebker, H. A., & Ellsworth, W. (2020). High-Pass Filters to Reduce the Effects of
838 Broad Atmospheric Contributions in SBAS Inversions: A Case Study in the Delaware
839 Basin. Waikaloa, HI, USA: 2020 IEEE International Geoscience and Remote Sensing
840 Symposium. DOI: 10.1109/IGARSS39084.2020.9324656.

841 Savvaidis, A., Lomax, A., & Breton, C. (2020). Induced Seismicity in the Delaware Basin, West
842 Texas, is Caused by Hydraulic Fracturing and Wastewater Disposal. *Bulletin of the*
843 *Seismological Society of America, 110*(5), 2225-2241. doi: 10.1785/0120200087.

844 Savvaidis, A., Young, B., Huang, G.-c., & Lomax, A. (2019). TexNet: A Statewide
845 Seismological Network in Texas. *Seismological Research Letters, 90*(4), 1702-1715. doi:
846 10.1785/0220180350.

847 Schultz, R., Skoumal, R. J., Brudzinski, M. R., Eaton, D., Baptie, B., & Ellsworth, W. (2020).
848 Hydraulic Fracturing-Induced Seismicity. *Reviews of Geophysics, 58*.
849 https://doi.org/10.1029/2019RG000695.

850 Sheng, Y., Ellsworth, W. L., & Pepin, K. S. (2020). Improved seismic depth and anaylisis from
851 moment tensor inversion in the Delaware Basin. *American Geophysical Union Fall*
852 *Meeting.* San Francisco (virtual).

853 Sheng, Y., Pepin, K. S., & Ellsworth, W. L. (submitted). On the Depth of Earthquakes in the
854 Delaware Basin - A Case Study along the Reeves-Pecos County Line. *The Seismic*
855 *Record*.

856 Skoumal, R. J., Barbour, A. J., Brudzinski, M. R., Langenkamp, T., & Kaven, J. O. (2020).
857 Induced Seismicity in the Delaware Basin, Texas. *Journal of Geophysical Research:*
858 *Solid earth, 125*(1). https://doi.org/10.1029/2019JB018558.

859 Staniewicz, S., Chen, J., Lee, H., Olson, J., Savvaidis, A., & Hennings, P. (Jan 27, 2021).
860 Cumulative and Transient Surface Deformation Signals in the Permian Basin. *Earth and*
861 *Space Science Open Archive ESSOAr*, (p. DOI:10.1002/essoar.10505979.1). Washington.

862 Staniewicz, S., Chen, J., Lee, H., Olson, J., Savvaidis, A., Reedy, R., . . . Hennings, P. (2020).
863 InSAR Reveals Complex Surface Deformation Patterns Over an 80,000 km^2 Oil-
864 Producing Region in the Permian Basin. *Geophysical Research Letters, 47*(21).
865 https://doi.org/10.18738/T8/AVDBOJ.

866 Starr, A. T. (1928). Slip in a crystal and rupture in a solid due to shear. *Mathematical*
867 *Proceedings of the Cambridge Philosophical Society, 24*(4), 489-500.
868 https://doi.org/10.1017/S0305004100014626.

869 Suckale, J. (2010). Moderate-to-large seismicity induced by hydrocarbon production. *The*
870 *Leading Edge, 29*(3). DOI:10.1190/1.3353728.

871 Teng, G., & Baker, J. W. (2020). Short-Term Probabilistic Hazard Assessment in Regions of
872 Induced Seismicity. *Bull. Seismol. Soc. Am., 110*, 2441-2453, doi: 10.1785/0120200081.

873 Texas Water Development Board (2013). *Groundwater Database (GWDB) Reports*. Retrieved
874 from Texas Water Development Board Groundwater Database:
875 http://www.twdb.texas.gov/groundwater/data/gwdbrpt.asp. Accessed 2020-06-15.

876 U.S. Geological Survey, Earthquake Hazards Program, 2017, Advanced National Seismic
877 System (ANSS) Comprehensive Catalog of Earthquake Events and Products: Various,
878 https://doi.org/10.5066/F7MS3QZH. Accessed 2020-09-15.
879
880 Weston, J., Ferreira, A. M., & Funning, G. J. (2012). Systematic comparisons of earthquake
881 source models determined using InSAR and seismic data. *Tectonophysics, 532-535*, 81-
882 81. doi:10.1016/j.tecto.2012.02.001.

883 Yeck, W. L., Hayes, G. P., McNamara, D. E., Rubinstein, J. L., Barnhart, W. D., Earle, P. S., &
884 Benz, H. M. (2017). Oklahoma experiences largest earthquake during ongoing regional
885 wastewater injection hazard mitigation efforts. *Geophysical Research Letters, 44*(2), 711-
886 717. doi:10.1002/2016GL071685.

887 Zebker, H. A. (2017). User-Friendly InSAR Data Products: Fast and Simple Timeseries
888 Processing. *IEEE Geoscience and Remote Sensing Letters, 14*(11), 2122-2126. doi:
889 10.1109/LGRS.2017.2753580

890 Zhai, G., Shirzaei, M., & Manga, M. (2021). Widespread deep seismicity in the Delaware Basin,
891 Texas, is mainly driven by shallow wastewater injection. *Proceedings of the National*
892 *Academy of Sciences, 118*(20). https://doi.org/10.1073/pnas.2102338118.

893 Zheng, Y., & Zebker, H. A. (2017). Phase Correction of Single-Look Complex Radar Images for
894 User-Friendly Efficient Interferogram Formation. *IEEE Journal of Selected Topics in*
895 *Applied Earth Observations and Remote Sensing, 10*(6), 2694-2701. doi:
896 10.1109/JSTARS.2017.2697861

897 Zhu, W., Allison, K. L., Dunham, E. M., & Yang, Y. (2020). Fault valving and pore pressure
898 evolution in simulations of earthquake sequences and aseismic slip. *Nat Commun,*
899 *11*(4833), doi: https://doi-org.stanford.idm.oclc.org/10.1038/s41467-020-18598-z.

900